# Behavior and mechanisms of Doppler wind lidar error in complex terrain: stable flow case study at Perdigão



# Behavior and mechanisms of Doppler wind lidar error in complex terrain: stable flow case study at Perdigão

**A Black[1], J K Lundquist[2,3], C Montavon[4], R Robey[2]**
[1] Vaisala France, 6a Rue René Razel, Saclay, France
[2] University of Colorado Boulder, Boulder, CO, USA
[3] National Renewable Energy Laboratory, Golden, CO, USA
[4] DNV, One Linear Park, Avon Street, Temple Quay, Bristol, BS2 0PS, UK

E-mail: andrew.hastingsblack@vaisala.com

**Abstract.** A numerical experiment is carried out investigating the magnitude of biases in ground-based lidar measurements in complex flow conditions. Biases assessed include those arising from flow curvature and from the interaction of turbulence with the wind field reconstruction (WFR) algorithms used by a WindCube lidars and anemometers. RANS-CFD and WRF-LES simulations were performed for the Perdigão Field Experiment site for a range of atmospheric conditions. Virtual anemometer and lidar data were generated for four locations: two near exposed ridge tops and two in low-speed regions in the valley. The LES data at these four locations show that the scalar inflation terms (the relation between scalar and vector averaged wind speed) for virtual lidar and virtual cups agree very well with predictions using perturbation theory. While the lidar errors vary greatly with location and height, the contribution from the flow curvature tends to be larger than the differences arising from scalar inflation. For one lidar/mast pair near the ridge top, comparisons between simulations and measurements are carried out for a resonant mountain wave event on June 14$^{\text{th}}$, 2017, and for the whole duration of the Perdigão campaign for winds perpendicular to the ridges. The lidar error during the mountain wave, a period of strong stability and low inversion height, is significantly larger than the campaign average. The sensitivity of the lidar error to atmospheric stability is confirmed by the RANS simulations, which suggests strong sensitivity of flow curvature error to stability conditions and to the shape of the wind speed profile near the top of the boundary layer.

## 1. Introduction

The wind flow in complex terrain can be difficult to simulate and to measure. Drastic changes in flow topology can occur due to interactions between atmospheric stability, the wind velocity profile, and the terrain. Some conditions can lead to separated flow regimes including cold pooling or recirculation zones, while others produce accelerated downdrafts in the lee of the terrain features [1]. Lidar wind field reconstruction algorithms (WFRs) assume homogeneous flow, but this assumption is broken in complex terrain due to flow curvature and vertical velocity differences at the different beams. Furthermore, both lidar and anemometer WFRs are sensitive to the Reynolds stresses and flow inclination.

The theory of lidar measurement errors in complex terrain has been explored in detail in [2] and [3]. Advancements have been made in the use of computational fluid dynamics (CFD) to

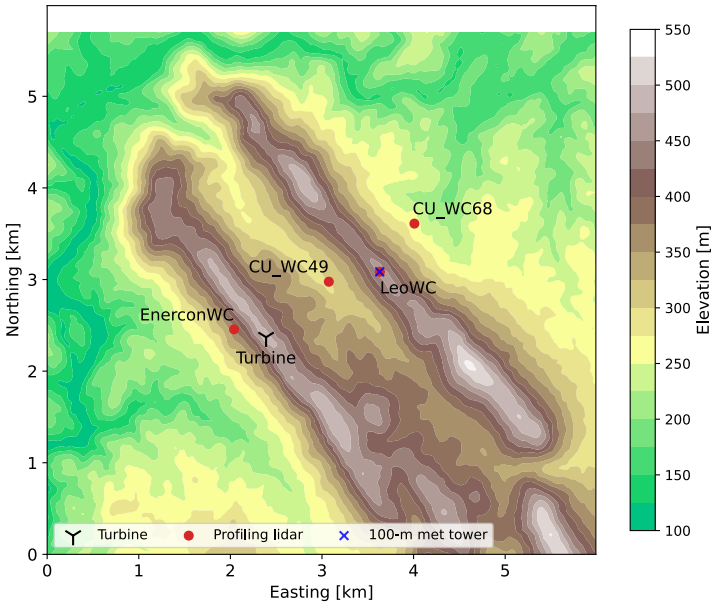


**Figure 1.** Perdigão site layout noting the location of the Enercon 82-m hub height turbine and profiling lidars: CU_WC49 (WindCube V1), LeoWC, and CU_WC68 (both WindCube v2).

model the flow above profiling lidar and apply corrections to the lidar data [4] [5]. Generally, these codes solve the Reynolds Averaged Navier-Stokes equations (RANS) and predict lidar WFR errors compared to the speed directly above the lidar. In moderately complex flows, these models show good skill and are commercially available and increasingly used for wind energy resource assessment. However, the upper performance envelope of these techniques is not well established. At highly complex sites, interactions between atmospheric stability (at the surface or higher up), the velocity profile, and the terrain can lead to drastic changes in flow topology. By examining correction skill at extreme sites, with different CFD approaches, we can learn more about the limits of applicability for wind energy applications and clarify opportunities for refinement.

We consider as a case study the Perdigão Field Experiment of 2016-2017 (Figure 1). Data collected from a WindCube V2 profiling lidar and a 100-m meteorological met mast equipped with ultrasonic sensors are compared against profiling lidar WFR errors predicted by a WRF-LES virtual lidar and by a commercial, RANS-based CFD. At LeoWC and three additional locations, we also quantify several sources of uncertainty in detail: (1) biases associated with scalar inflation (2) uncertainties arising from applying fixed flow curvature corrections to temporally changing flows, and (3) sensitivity of the simulations to boundary layer height, stability, and the input wind profile.

## 2. Methodology

### *2.1. RANS CFD simulation*

RANS simulations are carried out with the DNV-CFD model, a customised version of the STAR-CCM+ CFD software. The model solves the steady-state RANS equations, using the k-$\epsilon$ model for turbulence closure, with a modified set of constants [6]. DNV-CFD accounts for thermal stratification both within and above the boundary layer [6], [7]. This is done by including buoyancy effects in the vertical momentum equation and in the turbulence model, using a shallow Boussinesq formulation [8]. Stable and unstable surface conditions are modelled

with different approaches as described in [6] and [9]. The effect of the Coriolis force and the associated development of an Ekman spiral are also modelled. Where appropriate, the DNV-CFD model includes the Svensson resistive canopy model [10] designed to reproduce the turbulence generation and aerodynamic drag associated with forestry. Inputs to the canopy model include tree height, drag coefficient, and foliage density.

The model includes a module to extract flow curvature correction (FCC) factors for vertical profilers. For any solved flow condition, the FCC is calculated as: $FCC = V_{xy}/V_{rec}$, where $V_{xy}$ is the horizontal wind speed directly above the device, and $V_{rec}$ is the remote sensor-measured wind speed. FCC values are computed identically from the LES.

To test the FCC sensitivity, RANS simulations were carried out for the cases shown in Table 1, and the wind speed and potential temperature profiles shown in Figure 2. These cases include neutral (Case 1 and 3) and stable surface stability (L = 78 m, Cases 2, 4-7), and a range of inversion heights. Cases 1-4 use either high speed (HS) or low speed (LS) wind profiles, as typical for wind resource assessment CFD applications. Cases 5-7 have a pronounced low level jet (LLJ) profile. Cases 5-7 attempt to mimic the stable case modeled with the LES (as in [11]). All simulations target a wind direction of 215°.

The RANS simulations are solved on a domain spanning 38 km x 38 km x 17 km, centered at LeoWC. The terrain and tree height data for the central part of the domain were sourced from DTU [12], and had a combination of high resolution lidar scan, and 10 m resolution data. Further out, terrain data was sourced from SRTM [13], and roughness data from the ESRI 2020 10m resolution database [14]. The model was meshed with variable resolution. The horizontal resolution is 10-m within a 1 km radius from LeoWC, progressively coarsened to 25, 50, 100 m at radii of 4.5, 5.5 and 7.5 km from LeoWC, and to 200 m further out. Vertically, the first cell height is 2 m above the ground, with coarsening resolution through a prism layer made of 51 elements with a target thickness of 1800 m. Above the prism layer, a polyhedral mesh with a resolution of 200 m is used.

**Table 1.** RANS CFD cases configuration

| Case no. | Surface stability | Inversion height [m] | Wind speed profile |
|---|---|---|---|
| 1 | Neutral | 1350 | HS std |
| 2 | Stable | 500 | HS std |
| 3 | Neutral | 1050 | LS std |
| 4 | Stable | 500 | LS std |
| 5 | Stable | 500 | LLJ |
| 6 | Stable | 400 | LLJ |
| 7 | Stable | 300 | LLJ |

### *2.2. Large-eddy simulation*

The WRF-LES simulation follows the validated simulation of the case study of [11]. We follow the configurations therein, updated to WRFv4.3 and outputting 1-Hz data on which to run the virtual lidar model of [15]. The WRF-LES uses five WRF [16] nests from mesoscale down to LES scale (10 m horizontal grid spacing). The outer three nests are initialized on 13 June 2017, 18:00 UTC and allowed to spin up for 9 hours until 14 June 03:00. Next, the inner two LES are started and allowed to spin up for another 25 minutes, using a cell-perturbation method to speed up the generation of fine-scale turbulence. Usable LES data are between 14 June 2017,

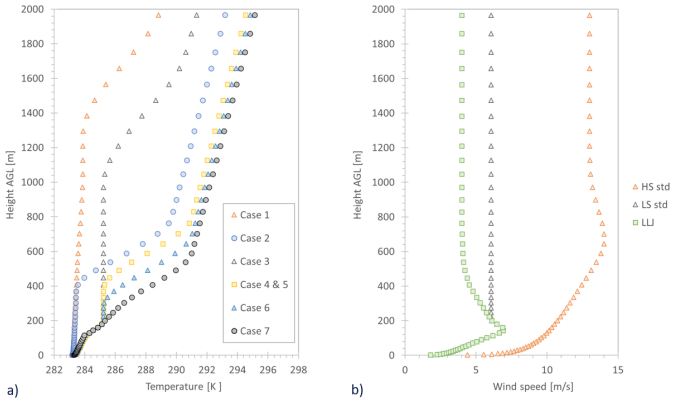


**Figure 2.** Inflow potential temperature and wind speed profiles for cases in RANS CFD

03:25 UTC to 05:15 UTC. These winds are southwesterly, just before dawn, configured as stable (L = 78 m). 1-Hz velocity time series are collected at points along the WindCube V2 profiling lidar's beam trajectories at each of the four locations. These data are projected onto the beams and combined via a range-weighting function to replicate the lidar observation system [15]. 1-Hz velocity time series are also collected at collocated, virtual 220-m met masts centered above each virtual lidar.

### *2.3. Wind statistics from the LES*

The virtual measurements are reconstructed into 1-Hz and 10-minute horizontal wind speeds following scalar, vector, and hybrid averaging of the WFR for the virtual lidars, and scalar and vector WFR for virtual masts at the center point of each measurement height[15]. Resulting profiles at the various locations are shown in Figure 4. For each virtual cup and lidar beam location, the Reynolds stresses are computed and tilt-corrected following methods described in [17].

*2.3.1. Virtual anemometer scalar inflation* For lidar and anemometer scalar averages, the time-average of the 1 Hz reconstructions generates a bias relative to vector averages as a consequence of Jensen's inequality:

$$\phi(E[X]) \leq E[\phi(X)] \tag{1}$$

for all convex functions $\phi$ [18]. The $l_2$ or Euclidian norm of the $u$- and $v$-components of the wind is a convex function; therefore, it is expected that scalar averages should always overestimate the corresponding vector averages. For wind measurements, this overestimation is called scalar inflation.

An estimate of the scalar inflation term has been derived previously using 2$^{\text{nd}}$ order Taylor series expansion [19]. To simplify the derivation for complex flows, we apply a 2$^{\text{nd}}$ order perturbation method proposed in [20].

The perturbation method derives the scalar inflation for arbitrary sensor geometries via: (a) measurement probe representation using $SO(3)$ rotation matrices; (b) flow representation using Reynolds decomposition and $SO(3)$ rotation for inclined flows; (c) WFR using Moore-Penrose pseudo-inverse matrix, and (4) the $l_2$ norm. This method yields a general form:

$$\overline{U}_{scalar} = U_{vector} + \frac{1}{2U_{vector}} \overline{\left\|\vec{U}'\right\|^2 \sin^2\theta} = U_{vector} + \frac{1}{2U_{vector}} \sum_{i,j=1}^{3} \left[\gamma_{ij} \circ \overline{\tau_{ij} \sin^2\theta}\right] \tag{2}$$

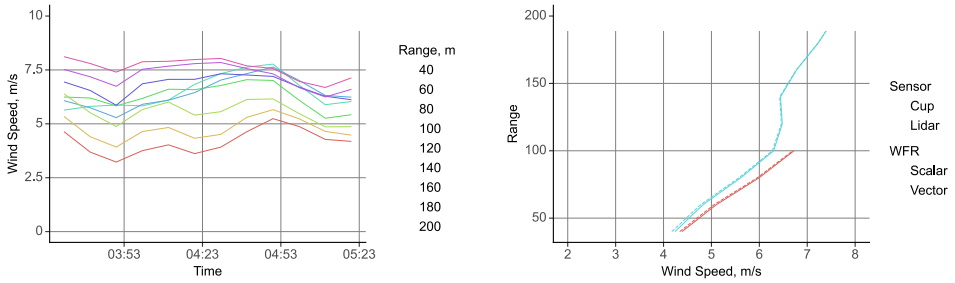


**Figure 3. (a)** LeoWC lidar observations using vector WFR on June 14$^{\text{th}}$, 2017. **(b)** 100 m met mast and LeoWC wind velocity profiles during June 14$^{\text{th}}$ mountain wave event. Note that the vector WFR (dashed line) closely matches scalar WFR.

where $\left\|\vec{U'}\right\|^2$ is the squared norm of the turbulent components measured along each beam transformed to the Cartesian reference frame, $\gamma_{ij}$ is the scalar inflation weighting matrix derived for the specific measurement and flow geometry, and $\circ$ is the Hadamard (element-wise) product of the two matrices. The final term can be expressed equivalently:

$$\overline{\tau_{ij}\sin^2\theta} = \overline{\tau_{ij}} * \overline{\sin^2\theta} + \mathrm{cov}(\tau_{ij}, \sin^2\theta) \tag{3}$$

This relationship demonstrates that covariance between the scalar inflation terms is mediated by the covariance between each Reynolds stress and $\sigma_{Dir}$. Entering the Reynolds stresses, inflow angles, and covariances into Equation 2, we predict the scalar inflation using:

$$\overline{U}_{scalar} = U_{vector} + \frac{1}{2U_{vector}} \sum_{i,j=1}^{3} \left[ \begin{bmatrix} \cos^2\theta_y & 0 & \sin\theta_y\cos\theta_y \\ 0 & 1 & 0 \\ \sin\theta_y\cos\theta_y & 0 & \sin^2\theta_y \end{bmatrix} \circ \overline{\tau_{ij}\sin^2\theta} \right] \tag{4}$$

where $\theta_y$ is the inflow angle at the measurement point, $\tau_{ij}$ are the tilt-corrected Reynolds stresses, and $\theta$ is the angle between the time-averaged wind direction and that of the 1-Hz fluctuation:

$$\theta = \tan^{-1}[(v_n - V)/(u_n - U)] \tag{5}$$

*2.3.2. Virtual lidar scalar inflation* For the virtual lidar, the scalar inflation term is computed using the Reynolds stresses and inflow angles computed from virtual anemometers at the beam locations. Non-diagonal Reynolds stresses and cross-terms between beams are dropped, yielding the form:

$$\overline{U}_{scalar} = U_{vector} + \frac{1}{8U_{vector}} \sum_{L=1}^{4} \left[ \sum_{i,j=1}^{3} \left[ \gamma_{ij,L} \circ \overline{\tau_{ij,L}\sin^2\theta_L} \right] \right] \tag{6}$$

where $L$ is each LOS beam, $\gamma_{ij,L}$ is a function of $\phi$, the lidar opening angle, $\theta_y$ and $\theta_z$, the flow inclination and azimuth angles as shown in [20].

*2.4. Campaign Measurement Data*

An identical dataset is created from measurements collected by the LeoWC WindCube V2 and the co-located 100 m met mast during the Perdigão experiment. This data is used to evaluate the skill of the CFD and LES predictions of lidar error, and it is shown in Figures 3 **(a)** and **(b)**.

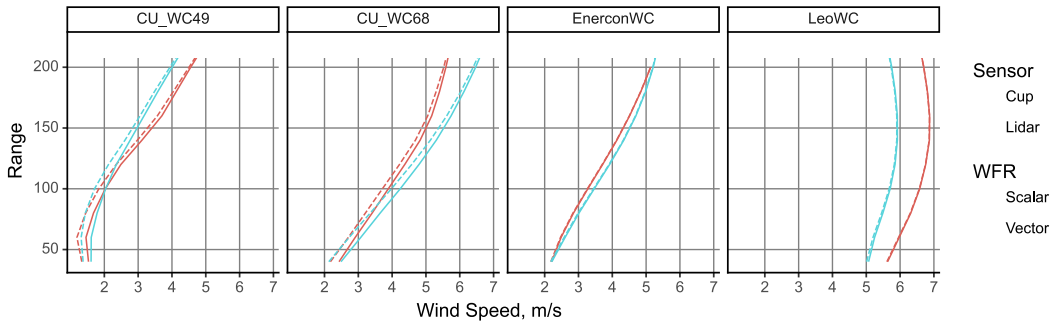


**Figure 4.** June 14th, 2017 LES averages of wind speed for uncorrected virtual lidar and virtual masts, with scalar and vector WFR

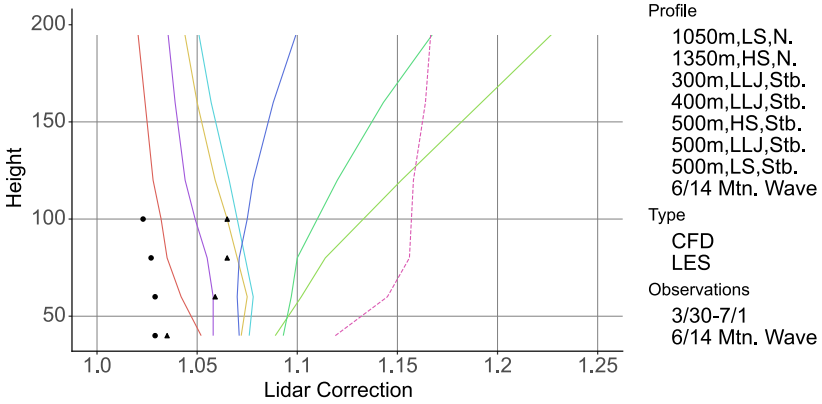


**Figure 5.** LES and CFD corrections compared to observed biases at LeoWC for the entire measurement campaign, and for the June 14th mountain wave event.

## 3. Results

### *3.1. CFD, LES, and Observed Lidar Correction Factors*

The lidar correction factors for the LeoWC instrument have been extracted from the LES and RANS simulations. They are compared to observed lidar biases in Figure 5.

Some interesting trends emerge from the RANS cases. Lowering of the inversion height (Case 1 to 2, 3 to 4, and 5 to 7) leads to an increase in the FCC. Keeping the same inversion height, but going from neutral to stable surface conditions while also reducing the wind speed (Case 1 to 3 and 2 to 4), causes a reduction in the FCC. It is not entirely clear which of the two causes dominates. With HS and LS profiles, the FCC tends to reduce with height, while a LLJ profile significantly increases FCC values with height.

The general increase in FCC in Cases 3-7 is directly linked with the magnitude of the mountain waves developing from the double ridges of the Perdigão site. The cross section of the vertical velocity in Figure 6 shows that Case 7 generates strong resonant waves. These waves lead to variation of the upflow angle across the lidar circle. In the resonant Case 7, the RANS CFD predicts that the lidar underestimates the wind speed by more than 20% at the height of 200 m. Case 3 (Neutral, BL = 1050 m, low speed) models the long-term correction for the 215° wind direction very well.

Virtual lidar 10-minute average wind speed biases averaged over the entire LES simulation period from each location are shown in Figure 7. The LES estimates biases of 11%-15% at

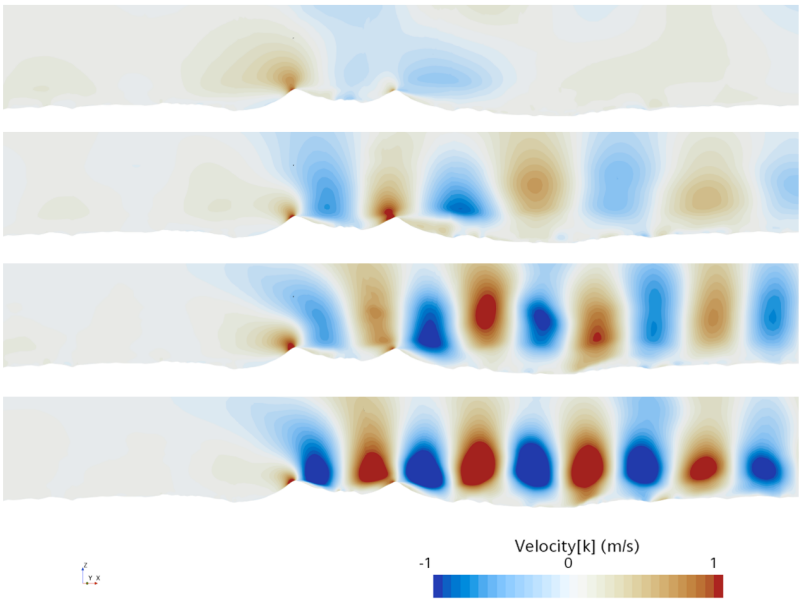


**Figure 6.** Cross section of vertical velocity along a plane through LeoWC, perpendicular to the main ridges. Results from the RANS simulations for the configurations 3, 4, 5 and 7.

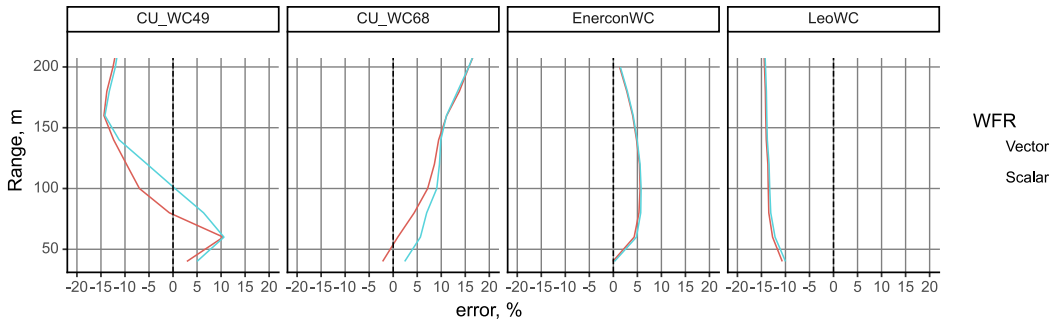


**Figure 7.** Uncorrected virtual lidar wind speed biases compared to virtual met masts. Both the lidar and anemometer speeds are reconstructed with the indicated WFR type.

the LeoWC site. This overestimation of the real lidar error by the LES indicates that the model exaggerates the curvature of the flow. In [11], the authors note that the wavelength of the mountain waves in the LES (1220 m) is 13% smaller than that observed by the long-range scanning lidars and other instruments (1410 m). A 13% reduction in wavelength induces a 13% increase in the local slope of a sinusoidal waveform via its derivative. This sensitivity demonstrates how changes in the wavelength and position of a mountain wave can modulate lidar measurement error. The relative change in correction factor with altitude is captured well by the LES, indicating that the change in curvature with altitude between 40 m and 100 m is well-modeled.

### *3.2. WFR Mismatch*

When validating lidar corrections using real data, cup anemometers using scalar WFR are often used as the ground truth reference (see [2] and [21]). The WindCube V2 is configured by default

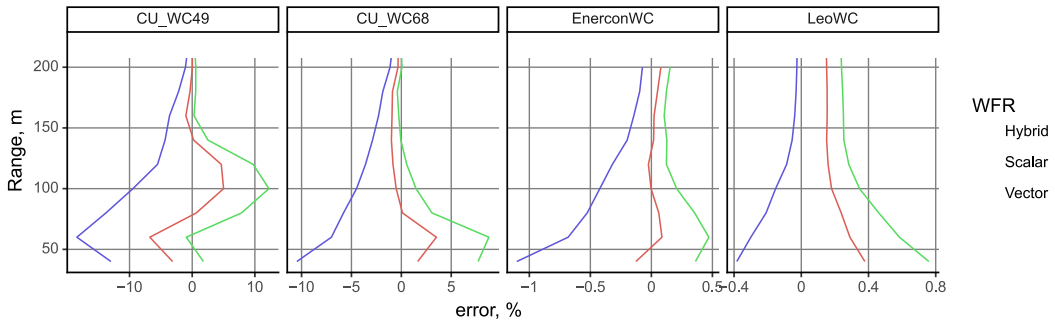


**Figure 8.** Errors in corrected lidar data arising from WFR mismatch between lidar, cup, and FCC. Indicated WFR is for the virtual lidar, and all are compared to anemometer scalar WFR.

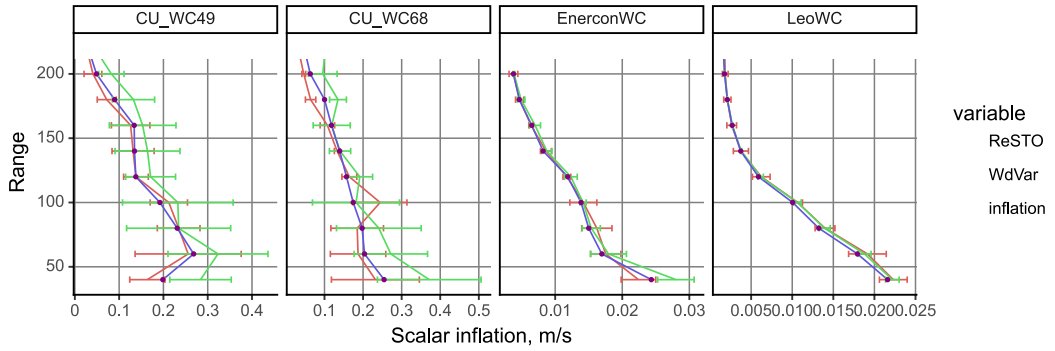


**Figure 9.** Virtual mast scalar inflation compared to predictions from perturbation theory and wind direction variance. Error bars indicate prediction residual standard error

to use scalar WFR. RANS-based lidar corrections can be understood as vector-like quantities, as they use converged vector components to estimate curvature and speed-up factors. The application of vector-like correction factors to scalar instruments creates an additional error shown in Figure 8. This mismatch explains some of the overestimation seen in [21]. As found in [15], the $\frac{2}{3}$:$\frac{1}{3}$ hybridization of scalar and vector WFR in the WindCube v2.1 effectively reduces the systematic scalar inflation error between lidar and cup anemometers.

### *3.3. Scalar Inflation Perturbation Theory*

Predictions from perturbation theory agree very closely with the scalar inflation terms from the LES virtual masts and lidars. Figure 9 shows the scalar inflation terms for the mast computed with Equation 4 ("ReSTO") and $0.5 * \sigma_\theta / U_{vector}$ ("WdVar") as proposed in [19]. Figure 10 shows the ReSTO and WdVar predictions for the lidar where $\sigma_\theta$ is computed using the 1 Hz lidar wind direction. In both Figures, the error bars are computed using the residual standard error from a linear fit between the predictions and the LES scalar inflation terms.

## 4. Discussion and Conclusions

We present a new model of scalar wind reconstruction errors using perturbation theory which is tested in an LES case with complex terrain. This model extends existing sensor error models [19, 22] to include the effects of complex flows, Reynolds stresses, and wind direction variance. These eight variables are treated simultaneously via the covariance between the Reynolds stresses and the wind direction fluctuation. Sensitivities may remain in anemometers or lidars due to flow

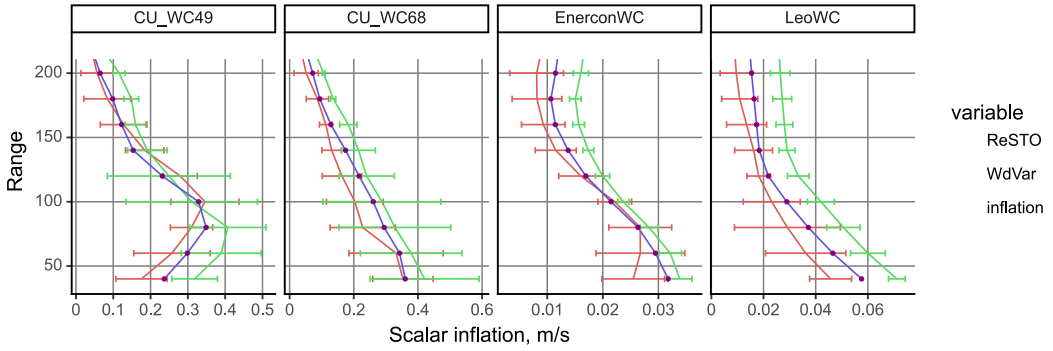


**Figure 10.** Virtual lidar scalar inflation compared to predictions from perturbation theory and wind direction variance. Error bars indicate prediction residual standard error

distortion from devices themselves, or other component sensitivities. These sensitivities could be identified as deviations from the idealized behavior demonstrated in the LES instruments.

When estimating sources of measurement sensitivity for device characterization or classification (see [23]), covariance between sensitive variables is often derived empirically between all pairs of candidate variables, and highly correlated variables are eliminated via a documented rubric. The scalar inflation term shows that measurement sensitivities to the Reynolds stresses should be estimated together, weighted according to the sensor measurement geometry ($\gamma_{ij}$), and their covariance computed with $\sin^2\theta$ rather than directly against one another. If further sensor sensitivities exist to Reynolds stresses, such as anemometer over-speeding or remote sensor volume averaging, these should be estimated in addition to the scalar inflation term.

Using the LES and CFD simulations, we have shown that the strongest driver for the flow curvature part of the lidar correction factor is not surface stability, but rather the stability conditions at the top and above the boundary layer. The inversion height and the presence of a LLJ can have a large impact on whether or not a mountain wave regime develops. This in turn affects the change in upflow angle across the lidar beams, and thus the flow curvature correction. For sites with frequent occurrence of very low inversions and LLJs, this suggests that to accurately capture the magnitude of the correction factor, a model should account for the effect of buoyancy in the vertical momentum equation. Without this, the model will not able to simulate mountain waves.

The observed differences between the CFD cases, the LES, and the observations indicate that lidar correction factors can be improved by modeling a wider range of conditions. Perdigão observations allow refinement of the input conditions for LES and RANS. Further developing this feedback loop between observations and modeling in order to better correct lidar measurements and to refine flow models of wind resources is a clear next step. The challenge will be to assess, for a given site, representative conditions to model and which measurements, perhaps beyond the typical lidar or met mast, could enable this refinement process. Both predicting scalar inflation in instruments and modeling flow curvature demonstrate the importance of treating linked parameters simultaneously.

## 5. Acknowledgments

This work was authored in part by the National Renewable Energy Laboratory, operated by Alliance for Sustainable Energy, LLC, for the US Department of Energy (DOE) under contract no. DE-AC36-08GO28308. Funding was provided by the US Department of Energy Office of

Energy Efficiency and Renewable Energy Wind Energy Technologies Office. The views expressed in the article do not necessarily represent the views of the DOE or the US Government. The US Government retains and the publisher, by accepting the article for publication, acknowledges that the US Government retains a nonexclusive, paid-up, irrevocable, worldwide license to publish or reproduce the published form of this work, or allow others to do so, for US Government purposes.

This material is based upon work supported by the U.S. Department of Energy, Office of Science, Office of Advanced Scientific Computing Research, Department of Energy Computational Science Graduate Fellowship under award number DE-SC0021110.

## References

[1] Stull R 1988 *An Introduction to Boundary Layer Meteorology* (Kluwer Academic Publishers)
[2] Bingöl F, Mann J and Foussekis D 2009 *Meteorologische Zeitschrift* 189–195 publisher: Schweizerbart'sche Verlagsbuchhandlung
[3] Klaas-Witt T and Emeis S 2022 *Wind Energy Science* **7** 413–431 ISSN 2366-7443 publisher: Copernicus GmbH URL https://wes.copernicus.org/articles/7/413/2022/
[4] Montavon C, Leask P, Tay K and I Y Kolbasi I Y 2022 *Wind Europe Conference, Bilbao*
[5] Black A, Mazoyer P, Wylie S, Debnath M, Lammers A, Spalding T and Schultz R 2020 Survey of Correction Techniques for Remote Sensing Devices in Complex Flow URL https://doi.org/10.5281/zenodo.4302363
[6] Bleeg J, Digraskar D, Woodcock J and Corbett J F *Wind Energy* **18** 369–383
[7] Bleeg J, Digraskar D, Horn U and Corbett J F 2015 *Proceedings of the EWEA Conference, Paris*
[8] Thunis P and Bornstein R 1996 *Journal of Atmospheric Sciences* **53** 380 – 397
[9] Bleeg J, del Hoyo M and Montavon C 2023 *WESC Conference, Glasgow*
[10] Svensson U and Häggkvist K 1990 *Journal of Wind Engineering and Industrial Aerodynamics* **35** 201–211 ISSN 0167-6105 URL https://www.sciencedirect.com/science/article/pii/016761059090216Y
[11] Wise A S, Neher J M T, Arthur R S, Mirocha J D, Lundquist J K and Chow F K 2022 *Wind Energy Science* **7** 367–386 ISSN 2366-7443 publisher: Copernicus GmbH URL https://wes.copernicus.org/articles/7/367/2022/
[12] Menke R 2021 email pointing to dropbox link for matlab file xyz_raw.mat, private communication
[13] SRTM Worldwide Elevation Data (1-arc-second resolution, SRTM Plus V3), accessed via GlobalMapper v25.0 URL https://lpdaac.usgs.gov/products/srtmgl1nv003/
[14] 2021 URL https://livingatlas.arcgis.com/landcover/
[15] Robey R and Lundquist J K 2022 *Atmospheric Measurement Techniques* **15** 4585–4622 ISSN 1867-8548 URL https://amt.copernicus.org/articles/15/4585/2022/
[16] Skamarock C, Klemp B, Dudhia J, Gill O, Liu Z, Berner J, Wang W, Powers G, Duda G, Barker D and Huang X y 2021 URL
[17] Wilczak J M, Oncley S P and Stage S A 2001 *Boundary-Layer Meteorology* **99** 127–150 URL http://link.springer.com/article/10.1023/A:1018966204465
[18] Jensen J L W V 1906 *Acta Mathematica* **30** 175–193 ISSN 0001-5962, 1871-2509 publisher: Institut Mittag-Leffler URL
[19] Rosenbusch P, Mazoyer P, Pontreau L, Allain P E and Cariou J P 2021 *Journal of Renewable and Sustainable Energy* **13** 063301 ISSN 1941-7012 URL https://doi.org/10.1063/5.0048810
[20] Black A, Delbos F and Cariou J P 2023 *WESC Conference, Glasgow*
[21] Stökl A, Koller S, Cordes J, Grüning O, Andrew B and Yoshimura A 2023 Report: IEA Wind TCP Task 32: Comparative Exercise on Ground Based Lidar in Complex Terrain URL https://doi.org/10.5281/zenodo.7598338
[22] Kristensen L, Hansen O F and Højstrup J 2003 *Wind Energy* **6** 321–331 (*Preprint* https://onlinelibrary.wiley.com/doi/pdf/10.1002/we.85) URL https://onlinelibrary.wiley.com/doi/abs/10.1002/we.85
[23] TC 88 2022 Wind energy generation systems - part 50: Wind measurement - overview Standard IEC 61400-50 International Electrotechnical Commission Geneva, CH URL https://webstore.iec.ch/publication/69215